#### ORIGINAL ARTICLE





# Thermosetting polymers in cold sintering: The fabrication of ZnO-polydimethylsiloxane composites

Arnaud Ndayishimiye<sup>1,2</sup> | Zane A. Grady<sup>1,2</sup> | Kosuke Tsuji<sup>1,2</sup> | Ke Wang<sup>1</sup> | Sun Hwi Bang<sup>1,2</sup> | Clive A. Randall<sup>1,2</sup>

<sup>1</sup>Materials Research Institute, The Pennsylvania State University, University Park, PA, USA

<sup>2</sup>Department of Materials Science and Engineering, The Pennsylvania State University, University Park, PA, USA

#### Correspondence

Arnaud Ndayishimiye, Materials Research Institute, The Pennsylvania State University, University Park, PA, USA. Email: axn536@psu.edu

#### **Funding information**

Murata Manufacturing Co., Ltd; AFOSR, Grant/Award Number: FA9550-16-1-0429; National Science Foundation, Grant/Award Number: DMR-1728634

### **Abstract**

This study reports the fabrication of the first ceramics-thermosetting polymer composites by the cold sintering process, for high ceramic volume fractions (v/v >95%). The (1-x) ZnO -x polydimethylsiloxane (PDMS) composites, with  $0.00 \le x \le 0.05$ , were cold sintered at 250°C, 320 MPa for 60 minutes. In situ densification studies conducted with the help of a semi-automated press revealed that the mechanisms driving the densification of the material changes with the polymer content. Relative densities of the (1-x) ZnO -x PDMS composites  $(0.00 \le x \le 0.05)$  were above 90%. Impedance spectroscopy of the composites yields insight into the ceramic-polymer interfaces within the sintered ZnO bulk and suggests long-range conduction governed by ZnO-PDMS interface properties for x = 0.03 and x = 0.05. The study also emphasizes on the complexities and opportunities of such ceramic-dominated ceramic-polymer composites.

### KEYWORDS

ceramics, cold sintering, densification, polymer, pressure solution creep

# 1 | INTRODUCTION

Recently, several studies have highlighted the possibility to fabricate ceramic-thermoplastic polymers composites by the cold sintering process (CSP). <sup>1-7</sup> The CSP is a technique that enables the fabrication of dense ceramics and ceramic-based composites at low temperature (<350°C), mainly based on a pressure solution creep mechanism (dissolution  $\rightarrow$  mass transport  $\rightarrow$  precipitation, following chemical potential gradients), induced by the presence of a transient liquid phase and uniaxial pressure.<sup>8-15</sup> CSP bridges the gap between processing temperatures of an important number of ceramics and polymers, offering a unique opportunity for the discovery, design, and fabrication of new composites with engineered grain boundaries. As an example, Randall et al investigated the potential of the CSP to several new ceramic-polymer composites, including the Li-ion battery electro- $\text{Li}_{1.5}\text{Al}_{0.5}\text{Ge}_{1.5}(\text{PO}_4)_3 - (-\text{CH}_2\text{CF}_2 -)_x [-\text{CF}_2\text{CF}(\text{CF}_3) -]_y,^{16}$   $\text{Li}_{1.5}\text{Al}_{0.5}\text{Ge}_{1.5}(\text{PO}_4)_3$  (LAGP) or  $\text{Li}_{1+x+v}\text{Al}_x\text{Ti}_{2-x}\text{Si}_v\text{P}_{3-x}$ <sub>v</sub>O<sub>12</sub> (LATP) with bis(trifluoromethanesulfonyl)imide (LiTFSI) salts showing similar room temperature conductivity (10<sup>-4</sup> S·cm<sup>-1</sup>) as conventionally sintered ceramics, <sup>17</sup> Li-ion cathode LiFePO<sub>4</sub>-Polyvinylidene fluoride with enhanced electrochemical performances, 18 semiconductor V<sub>2</sub>O<sub>5</sub>-poly(3,4-ethylenedioxythiophene) polystyrene sulfonate composites with engineered mechanical, thermal, and electronic properties.<sup>19</sup> These studies highlight the new opportunities for high ceramic volume fraction (v/v >95%) ceramic-thermoplastic polymer composites enabled by cold sintering. These studies also demonstrated the retention of both the ceramic and polymeric functional properties in the bulk composite, made possible by the targeted grain boundary functionalization with the polymeric additive. To date, only thermoplastic polymers have been used in the fabrication of cold sintered composites. However, thermosetting polymers comprise a large fraction of the contemporary polymeric research and industrial applications. <sup>20,21</sup> One of the main advantages of thermosetting polymers is the possibility to start with a low viscosity liquid prior to curing, enabling facile processing and homogenous distribution. <sup>22,23</sup> This attribute can lead to highly cross-linked network after being fully cured within the same temperature ranges as typical CSPs; overtly introducing the possibility of a cold sintering mediated in situ polymer cross-linking process. Polydimethylsiloxane (PDMS) is one such thermosetting polymer of industrial relevance, being widely employed in electronics, biomedical, cosmetic, food and also known for its good moldability, cost-effectiveness, chemical, and mechanical robustness. <sup>24–29</sup>

Cold sintering has been extensively applied to ZnO<sup>30,31</sup> as well as multiple ceramic-polymer systems, such as ZnO-PTFE,<sup>2</sup> so it is sensible to extend CSP to thermosetting polymers by first investigating a ZnO-thermoset composite. Accordingly, this work is concerned with the ZnO-PDMS composite fabricated via cold sintering. Previous studies have explored the ZnO-PDMS composite system from an electrical property perspective, where the ZnO was introduced as a nanofiller (eg, nanorods, nanoparticles) to augment a PDMS matrix.<sup>32,33</sup> In such a nanocomposite system where the characteristic electrical responses of the constituent materials occur at different length/time scales, impedance spectroscopy has proven a powerful method to elucidating the interfacial and bulk electrical responses.<sup>34,35</sup>

This study also investigates the influence of the volume fraction of polymer on the densification behavior, final density, microstructure, and electrical properties of the cold sintered (1 - x) ZnO - x PDMS composites (with x = 0.00, 0.01, 0.03, and 0.05). The impedance response of the ZnO-PDMS composites introduced in this work illustrates the unique interfacial effects that arise in such cold sintered ceramic-polymer nanocomposite systems. The study also emphasizes on the complexities and opportunities of such ceramic-dominated ceramic-polymer composites.

### 2 | EXPERIMENTAL SECTION

### 2.1 | Materials

ZnO (99.9%, Alfa Aesar), with particle size of 40-100 nm, was used as starting powder (Figure S1). Hydroxy terminated PDMS ( $\sim 65 \text{ cSt}$ ,  $\overline{M}_n = \sim 1430$ , Sigma Aldrich), prepared with a Sylgard<sup>®</sup> cross-linking agent with a molar ratio of 10:1, was used as a polymer. The appropriate amount of powders and liquid polymer were carefully mixed to fabricate (1-x) ZnO -x PDMS composites with different volume fractions: x = 0.00, 0.01, 0.03, and 0.05.

# 2.2 | CSP and pellet preparation

For each sample, (1 - x) ZnO - x PDMS was prepared by first mixing ZnO with 20 wt% of a 2 mol·L<sup>-1</sup> acetic acid solution prepared from glacial acetic acid (VWR, VW0125-3, 17.6 mol·L<sup>-1</sup>). ZnO powder and acetic acid were manually mixed with in an agate mortar and pestle for 3 minutes. The appropriate amount of low viscosity PDMS polymer/crosslinking agent mixture was then added in the wet powder and mixed for 2-3 minutes. The mixture was then poured into a 12.7-mm-diameter stainless steel die. Experiments were then performed with a device composed of (a) an ENERPAC press able to automatically maintain the pressure constant with the help of an electric hydraulic pump, (b) a dilatometer with a Keyence GT2-H32 Digital Contact Sensor. 36 The mixture was first pressed under 320 MPa at room temperature for 10 minutes to allow further particle rearrangement, the temperature was then increased to 250°C with a 20°C·min<sup>-1</sup> average heating rate. The mixture was maintained in the die at 250°C for 60 minutes. After the dwell, the pressure was naturally released as the system was cooling down.

# 2.3 | Material characterizations

# 2.3.1 | X-ray diffraction

Phases of sintered pellets were characterized by X-ray diffraction (XRD) with a PANalytical Empyrean diffractometer, operating at 45 kV and 40 mA. Diffraction signals were collected between 20 angles of 20° and 60°, using a step size of  $0.026^{\circ}$  with a Cu K $\alpha$  radiation.

# 2.3.2 | Density measurements

Final pellets

Real densities ( $\rho_{\rm real}$ ) of cold sintered pellets were measured by He gas pycnometer (Micromeritics Accupyc II 1340), using an equilibration pressure of 0.0050 psig·min<sup>-1</sup> for high precision measurements. Bulk densities ( $\rho_{\rm bulk}$ ) were obtained by the Archimedes method, using ethanol as the liquid medium at room temperature. The mass of the dry pellet ( $m_{\rm d}$ ) was first measured. Then the sample was immersed in ethanol for 2 minutes to fill open pores with the fluid, prior to measuring the mass of the sample in the liquid medium ( $m_{\rm l}$ ). The sample surface was then gently wiped to remove any excess on the surface and the mass of the sample saturated with liquid ( $m_{\rm s}$ ) was measured in air.

The bulk density was calculated by the following relation:

$$\rho_{\text{bulk}} = \frac{m_{\text{d}} \cdot \rho_{\text{fluid}}}{\left(m_{\text{s}} - m_{\text{l}}\right)}$$



The relative density  $(d_{rel.})$  was then calculated with the following relation:

$$d_{\rm rel.} = \frac{\rho_{\rm bulk}}{\rho_{\rm real}}$$

*In situ data*<sup>37</sup>

The thermal behavior of the empty die is first evaluated with the defined sintering temperature and pressure schedules. This is then subtracted from the sample-loaded die during sintering. The obtained time-dependent shrinkage information, s(t), was converted into relative density  $d_{\rm rel.}(t)$ , using the real density of the final material  $\rho_{\rm real-f}$  following the equation:

$$d_{\text{rel.}}(t) = \frac{m_{\text{f}}}{\pi \times r_{\text{f}}^2 \times (t_{\text{f}} + |s(t)|) \times \rho_{\text{real-f}}}$$

where  $m_{\rm f}$ ,  $r_{\rm f}$ , and  $t_{\rm f}$  are respectively the mass, the radius and the thickness of the final pellet. This calculation is based on three major assumptions: (a) the true density is invariant during the temperature and pressure schedules, (b) the cool down after the dwell does not have a significant effect on the final density, (c) the powder does not escape from the die during the densification.

# 2.3.3 | High-resolution electron scanning microscopy

Scanning electron microscopy (SEM) was performed on a FEI Nova NanoSEM 630, with accelerating voltages of 7 kV. Analysis was made on iridium-sputtered fractures of bulk densified samples. The grain size measurement was performed with the freeware Image J,  $^{38}$  preferentially on the major axis ( $d_{\text{max}}$ ) of at least 150 grains. The measurements of the minor axis ( $d_{\text{min}}$ ) were also made to evaluate the aspect ratio of grains, using  $d_{\text{max}}/d_{\text{min}}$ .

# 2.3.4 | High-resolution transmission electron microscopy

Samples for transmission electron microscopy (TEM) analysis were prepared using a FEI Helios 660 focused ion beam (FIB) system. A thick protective amorphous carbon layer was deposited over the region of interest then Ga<sup>+</sup> ions (30 kV then stepped down to 1 kV to avoid ion beam damage to the sample surface) were used in the FIB to make the samples electron transparent for TEM images. A FEI Titan G2 (60-300 kV) electron microscope equipped with a superX EDS system was used, with an accelerating voltage of 300 kV for high-resolution imaging (HR-TEM), high-angle annular

dark-field scanning transmission microscope (STEM), and energy dispersive spectroscopy (EDS) mapping.

# 2.3.5 | Brunauer-Emmett-Teller (BET)

The Brunauer-Emmett-Teller (BET) surface area measurements of the cold sintered pellet were obtained by  $N_2$  gas molecule adsorption after the sample degassing at  $80^{\circ}$ C for 8 hours (ASAP 2020 Automated Surface Area and Porosimetry System).

# 2.3.6 | Fourier Transformed infrared spectroscopy

FTIR experiments were conducted using a Bruker Vertex 70 FTIR spectrometer with an Attenuated Total Reflection accessory, equipped with a liquid nitrogen-cooled MCT detector. Spectra were collected at room temperature and were obtained from an average of 200 scans in the wavelength range of 500-4000 cm<sup>-1</sup>.

### 2.3.7 | Electrical characterization

Impedance spectroscopy was performed on the samples of designated volume fractions of PDMS. Samples were polished by hand to 1200 grit and sputtered coated (EMS 150R-S, Quorum Technologies, East Sussex, UK) with circular platinum (Kurt J. Lesker) electrodes of approximately 80 nm thickness and 0.1 cm<sup>2</sup> area. Prior to measurement, the samples were dried under vacuum at 75°C for at least a week to evaporate any absorbed moisture and ensure the polymer cross-linking reaction had proceeded to such a degree that only small fluctuations in the AC (alternative current) bias response were observed (Figure S2). To minimize the secondary effect of absorbed ambient moisture on the impedance of ZnO-PDMS, most measurements were taken on the same day. The change in impedance during drying, indicating that the long drying time is necessary to ensure no further chemical changes are induced by additional drying. An impedance analyzer (ModuLab XM MTS) was used to collect impedance measurements from 1 MHz to 0.05 Hz with an applied voltage of 0.5 V. Impedance measurements at different temperatures were collected inside a Delta 9023 oven with a nominal equilibration time of 15 minutes.

# 2.3.8 | Differential Scanning Calorimetry

A TA Instruments Q2000 MDSC® (Modulated Differential Scanning Calorimeter) was used to conduct thermal studies,

under a 50 mL/min nitrogen flow. Cold sintered samples weighing 20-22 mg and  $\sim$ 8  $\mu$ L of neat PDMS were used for analyses.

### 3 | RESULTS AND DISCUSSION

# 3.1 | Densification of (1 - x) ZnO - x PDMS composites

The densification behavior of (1 - x) ZnO - x PDMS composites was evaluated with shrinkage information obtained with a semi-automated press system, equipped with a dilatometer. Figure 1A shows the evolution of the relative density with time. The green density is read at t = 0 minutes and is obtained after 10 minutes of room temperature compaction at 320 MPa. It increases with the volume fraction of PDMS, from 54% to 64% for x = 0.00 and x = 0.05, respectively. Prior to sintering, the liquid polymer fills some pores and slightly contributes to the enhancement of particles sliding and rearrangement. Densification curves can be divided into three main steps (inset Figure 1A). (a) Step 1 occurs up to t = 4 minutes of the thermal cycle and corresponds to the particle rearrangement, following the die expansion when the temperature increases. The rearrangement time for the composite with x = 0.01 is shorter than the one of pure ZnO (with x = 0.00), as PDMS decreases friction between particles and facilitates the rearrangement. An additional contribution (noted \* on the inset of the Figure 1A) is observed for the composites with x = 0.03 and x = 0.05. This may be associated with the redistribution of the polymer following a perturbation resulting from the bulk movement of particles. (b) Step 2 occurs up to t = 7 minutes of the thermal cycle and corresponds to stage where most of the mechano-chemical effects of cold sintering, driven by the pressure solution creep, take place. The pressure solution creep mechanism is induced by the presence of a transport liquid phase and uniaxial pressure. It has three main steps (dissolution, mass transport, and precipitation) and is driven by chemical potential gradients. 12,39,40 It is observed that most of the densification takes place at this stage, as well as the evaporation of the excess solvent present in the system. Curve segments of all samples are parallel, and it may be indicative of a pressure solution creep mechanism occurring on the same material (ZnO) and at equivalent densification rates. Most of the densification of ZnO and (1 - x) ZnO - x PDMS composites takes place at this stage as the relative density is at ~90% or above for all samples. (c) Step 3 includes the dwell time. At this stage, a slight increase in relative density with time is only observed for the pure ZnO system, leading to a relative density of 98.3% (Figure 1A,B). Indeed, for pure ZnO at this stage, molecules composing the solvent confined between two grains are driving the further increase in relative density. Chemical reactions taking place are mainly based on the dissociation of acetic acid molecules by their deprotonation either by surface oxygen, bridging hydroxyl on the ZnO surface. <sup>41–43</sup> In the presence of PDMS, the relative density is quasi-constant, as it may act as a diffusion barrier.

However, it is obvious that all the materials are densified after the sintering cycle as evidenced by the relative densities above 90% (Figure 1B) and the surface area evolution, starting from 13.6 m<sup>2</sup>·g<sup>-1</sup> for the initial ZnO powder to a value lower than 2 m<sup>2</sup>·g<sup>-1</sup> for all (1 - x) ZnO - x PDMS cold sintered materials (Figure 1C).

During the pressure solution creep (Figure 1D), the dissolution is enhanced at the contact points between ceramic grains, where is also trapped a thin layer of the transient liquid phase (or transient liquid phase and polymer in the case of composites). The species dissolved at the solid/liquid interface are transported following a chemical potential gradient existing between the liquid phase with a high concentration of solute  $(\mu_{1,1})$  and the liquid phase with a lower concentration of solute  $(\mu_{1,2})$ . Gratier et al<sup>39</sup> described the transport flux as the diffusion coefficient (D) times the gradient in chemical potential (Equation [1]). The authors also note that the factor  $\frac{dc}{du}$  may be nonlinear, but that more work may be

necessary to precisely quantify it.

$$J_r = -D\left(\frac{\mathrm{d}c}{\mathrm{d}\mu}\right) \nabla \mu_{\mathrm{T}} \tag{1}$$

Furthermore, Ware et al<sup>44</sup> have shown that the diffusion coefficient of molecular species in a polymer-solvent mixture follows a scaling law, resulting from the second Fick's law and given by Equation (2):

$$D = D_0 \exp^{-ac^{\nu}} \tag{2}$$

where D is the diffusion coefficient at polymer concentration c,  $D_0$  is the diffusion coefficient in the absence of a polymer,  $\nu$  is a constant which depends on the ionic strength of the solvent, a is a constant which shows little sensitivity to polymer charge density or ionic strength.

It is reasonable to assume that the decrease in the diffusion coefficient in presence of polymers leads to a lower mass transport flux. The mass transport can thus be considered as the rate-limiting step during the cold sintering of (1 - x) ZnO – x PDMS composites.

Given that the thickness of the liquid phase(s) trapped between particles is a function of the effective local contact pressure, <sup>45</sup> one can assume that in directions other than the one of the applied pressure, two main effects may lead to a thicker polymer layer between two grains and thus limit the mass transport limitation: (a) the local stress at grain contacts whose surfaces are not orthogonal to the applied pressure

**FIGURE 1** Evolution of the: (A) relative density of cold sintered (1-x) ZnO -x PDMS composites with the time. The red zone delimits the heating ramp time, (B) relative density, and (C) surface area with the volume fraction of PDMS. (D) Schematic of particle-particle contacts in the ZnO-PDMS system  $\Delta\mu_{\rm D}, \Delta\mu_{\rm T}$ , and  $\Delta\mu_{\rm P}$  are driving forces of dissolution, mass transport, and precipitation, respectively. PDMS, polydimethylsiloxane

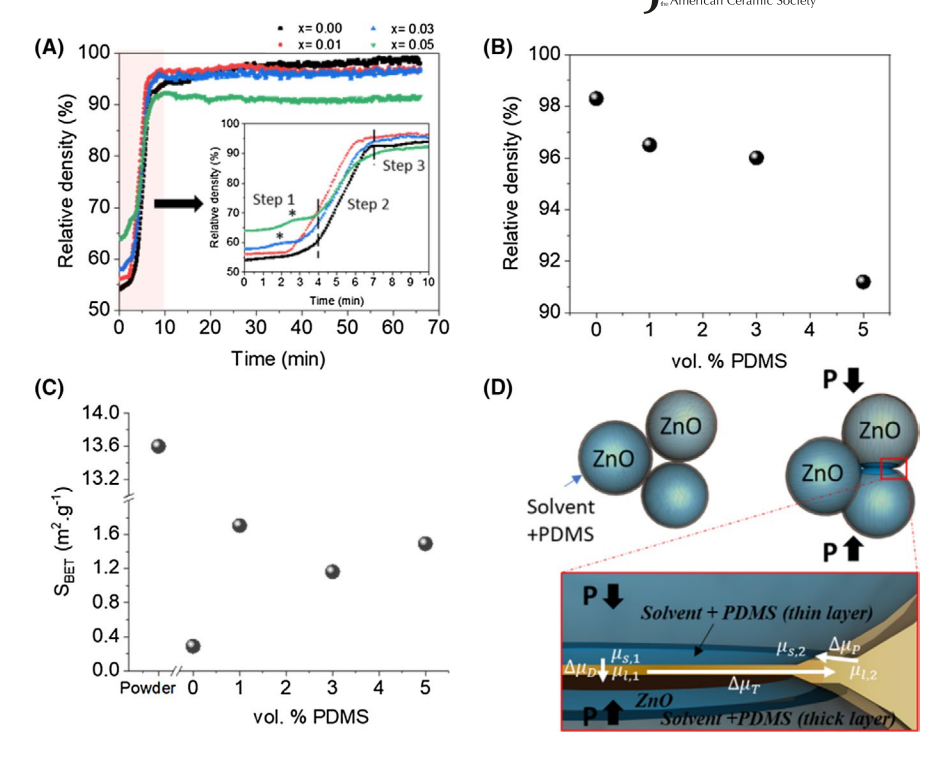
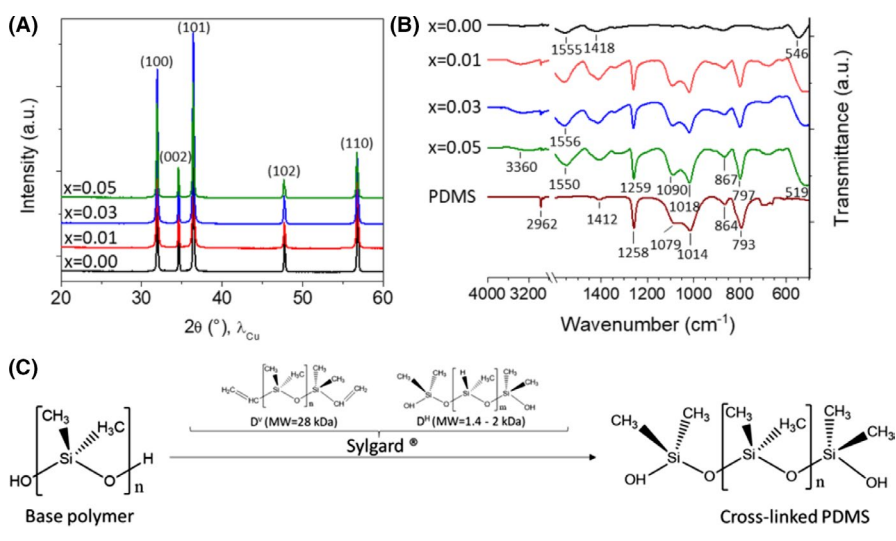


**FIGURE 2** (A) X-ray diffraction patterns, (B) FTIR spectra of cold sintered (1-x) ZnO -x PDMS composites, (C) Thermal cross-linking reaction of PDMS in the presence of Sylgard<sup>®</sup>, with  $n_{\text{(base polymer)}} \ll n_{\text{(cross-linked PDMS)}}$ . PDMS, polydimethylsiloxane



experience significantly less pressure and a commensurately reduced driving force for densification, (b) these aforementioned areas of lower stress also act as areas for polymer accumulation for material extruded out from the more highly constrained contact points between ceramic grains, further restricting the densification process (Figure 1D).

# 3.2 | Structural and microstructural analyses

Figure 2A shows that the structure is maintained for all (1-x) ZnO – x PDMS cold sintered composites. XRD patterns of cold sintered samples are similar and highlight ZnO

as the only crystalline phase (PDF No. 98 000 0483). There is no obvious evidence of interphase formation or secondary phase. The presence of PDMS polymer in composites is evidenced by FTIR analysis (Figure 2B). Infrared bands located at 2962, 1412, and 1258 cm<sup>-1</sup> are respectively assigned to asymmetric C-H stretching in -CH<sub>3</sub> functional group, asymmetric and symmetric deformation vibration of CH<sub>3</sub> group in the methyl-silicon compound Si-CH<sub>3</sub>. The Si-O stretching vibration in -(Si-O)<sub>n</sub>- siloxane backbone is identified by the bands located at 1014 and 1079 cm<sup>-1</sup>. In siloxanes, the band at 796 cm<sup>-1</sup> is assigned to stretching vibration of Si-C. The rocking vibration of this latter bonding is located at 864 cm<sup>-1</sup>. Year By FTIR, ZnO is mainly identified by the presence of bands located at 546, 1418,

and 1555 cm<sup>-1</sup> assigned to Zn-O stretching vibrations, symmetric and asymmetric stretching of carboxylate group -COO- of residual acetate anions chemically attached to ZnO surface, respectively.<sup>48</sup> The wide O-H stretching band is located at 3360 cm<sup>-1</sup>.

The Zn-O stretching band, initially located at 546 cm<sup>-1</sup> for cold sintered ZnO, shifts at least 25 cm<sup>-1</sup> from its initial position. It was shown by Rose et al<sup>49</sup> that polymer chains can strongly adsorb on particle surfaces even when a contact pressure as low as 10 kPa is applied. The magnitude of the shift observed for the cold sintered (1 - x) ZnO - x PDMS let us assume that hydrogen bonds may form at the between the ZnO surface and PDMS. 50 Between the FTIR spectra of cold sintered ZnO and (1 - x) ZnO - x PDMS composites, intensities of bands located at 3360, 1555, and 1418 cm<sup>-1</sup> increase, suggesting the presence of more residual solvent on the composite's ZnO surfaces. Between the FTIR spectra of neat PDMS and cold sintered (1 - x) ZnO - x PDMS composites, the weak band at 2962 cm<sup>-1</sup> decreases in intensity and all the infrared bands, except the band located at 1258 cm<sup>-1</sup>, shift at least 3 cm<sup>-1</sup> from their initial positions. The most important shift, of 11 cm<sup>-1</sup>, is observed for the band attributed to Si-O stretching in -(Si-O)<sub>n</sub>- siloxane backbone initially located at 1079 cm<sup>-1</sup>. These changes suggest that a cross-linking reaction, following the equation presented at Figure 2C, takes place during the CSP.

Differential Scanning Calorimetry was used to further investigate qualitatively the cross-linking in cold sintered specimen (Figure 3). Cold sintered ZnO and neat PDMS were analyzed. Furthermore, 0.85ZnO-0.15PDMS composites were prepared to have enough heat flow originating from the polymer. Two composite specimens were prepared following the procedure detailed in Sections 2.1 and 2.2, with sintering times of 60 and 180 minutes. In the temperature range explored (200-270°C), no obvious peak is observed for the ZnO sample.

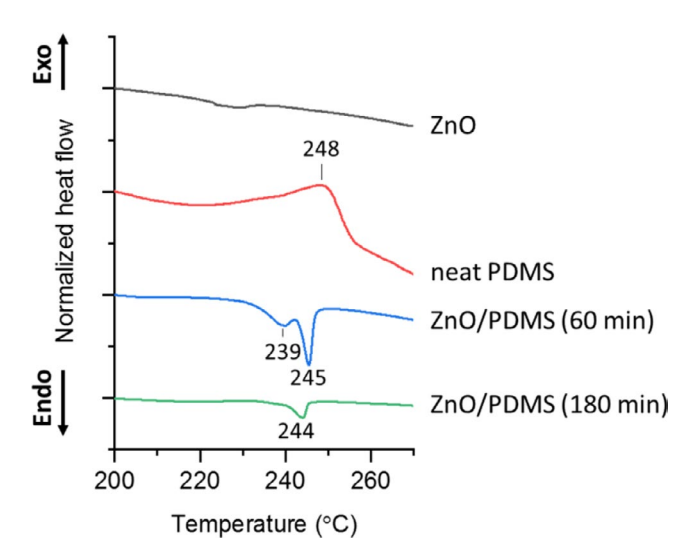


**FIGURE 3** DSC of ZnO, neat PDMS and 0.85ZnO-0.15PDMS composites sintered for 60 and 180 min. PDMS, polydimethylsiloxane

An exothermal peak, indicative of a cross-linking reaction,<sup>51</sup> is observed at 248°C for the neat PDMS. For the 0.85ZnO-0.15PDMS composite cold sintered for 60 minutes, two initial decomposition temperature (IDT)<sup>52,53</sup> peaks are observed at 239 and 245°C and may be related to the initial degradation of cross-linked PDMS networks with different cross-linking degrees. After 180 minutes of cold sintering, only one IDT peak is observed, indicating that the gross degree of cross-linking in the PDMS may be more uniform with higher sintering time.

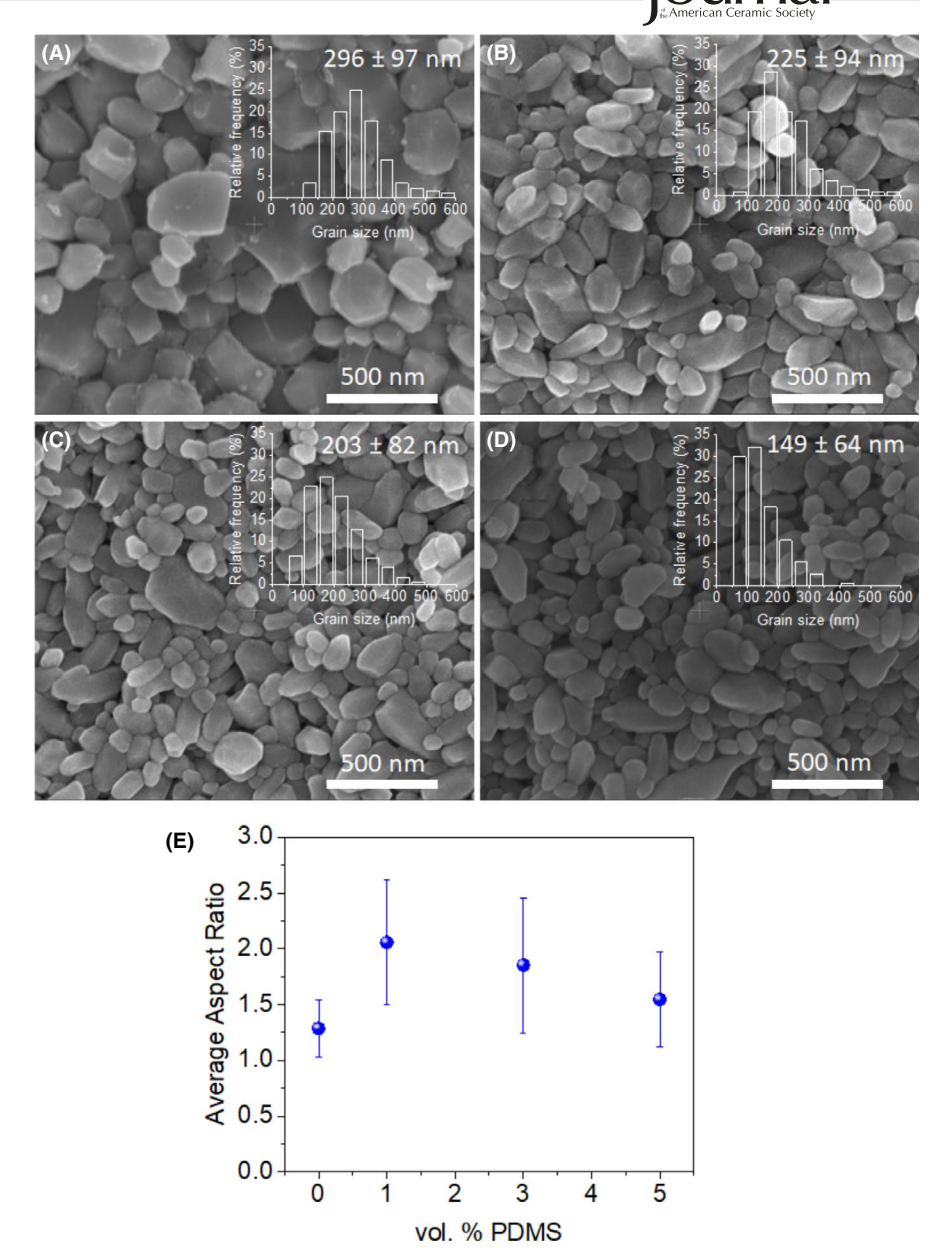
Scanning electron microscopy images show the microstructural evolution of cold sintered (1-x) ZnO -x PDMS composites (Figure 4A-D). When x=0.00, the average grain size is  $296 \pm 97$  nm, which is consistent with previous studies involving the CSP of ZnO $^{30,31,54}$  and obviously higher than the initial particle size estimated at  $79 \pm 37$  nm (Figure S1). The addition of PDMS leads to a change in grain size distribution and average grain size, with  $225 \pm 94$ ,  $203 \pm 82$ , and  $149 \pm 64$  nm for x=0.01, 0.03, and 0.05, respectively (Figure 4). The polymer may act as a diffusion barrier, suppressing the grain growth at the last stage of CSP.

Despite the diffusion barrier presented by the presence of PDMS, the ZnO matrix is still densified where the pressure is sufficient to extrude the polymer from between grains and create ZnO-ZnO interfaces and thereby enable densification. The morphological change in grain shape and the presence of equilibrated dihedral grain contacts observed in SEM images (Figure 4B-D) irrespective of volume fraction of PDMS supports this. SEM analyses also show a change in the aspect ratio of grains. In the Figure 4E, the aspect ratio is calculated using  $d_{\text{max}}/d_{\text{min}}$ . The aspect ratio of the initial powder was estimated at  $1.52 \pm 0.48$  (Figure S1). After sintering and in the absence of PDMS, the average aspect ratio is close to 1 (ie, isotropic grains), at a value of  $1.29 \pm 0.26$ . The grain anisotropy is increased by adding PDMS; the highest average aspect ratio of  $2.06 \pm 0.56$  being observed for x = 0.01. For this case where x = 0.01, the transport flux during pressure solution is still relatively sufficient to drive grain growth due to a low concentration of polymer. The slight increase in polymer thickness in less stressed areas limits the diffusional transport in directions other than the one of applied pressure. The anisotropy then slightly decreases when x > 0.01 as the transport flux at contact points between two grains is also decreased due to the increased diffusion barrier presented by a larger concentration of PDMS.

These observations confirm that in the presence of a thermosetting polymer, the grain growth takes place following dissolution-precipitation creep and additional diffusion-controlled growth mechanisms such as Ostwald ripening or colescence<sup>55</sup> that may preferentially occur in the direction of pressure, where the stress at particle contacts is the highest.

The composite 0.97 ZnO - 0.03 PDMS was investigated with high-resolution STEM and EDS mapping (Figure 5A-h).

**FIGURE 4** SEM images of cold sintered (1 - x) ZnO - x PDMS composites with: (A) x = 0.00, (B) x = 0.01, (C) x = 0.03, and (D) x = 0.05. (E) Average aspect ratio  $(d_{\text{max}}/d_{\text{min}})$  of grains with the volume fraction of PDMS. PDMS, polydimethylsiloxane; SEM, scanning electron microscopy



The microstructure observed by SEM (Figure 4C) is consistent with the low magnification TEM image (Figure 5A), as ZnO grains with sizes ranging between ~50 nm and several hundreds of nm are observed. The main microstructural configuration can be summarized by the presence of ZnO/ZnO interfaces as well as ZnO/PDMS/ZnO ones (Figure 4B). The densification of the ZnO matrix by pressure solution creep (see Section 3.1) implies the presence of ceramic/ceramic contacts. In (1 - x) ZnO - x PDMS composites, the presence of these latter is confirmed by the HR-TEM image in Figure 5D, which highlights the presence of a sharp grain boundary between two ZnO grains. The Figure 5C shows a HR-TEM image, highlighting the presence of PDMS polymers. To clearly distinguish the location of PDMS, EDS mapping under STEM mode was also performed (Figure 5G,h), confirming its presence at most of the ZnO grain boundaries (Figure 5H). This observation is consistent with the ZnO/PDMS/ZnO configuration previously discussed (see Section 3.1), that contributes to the grain growth limitation in (1 - x) ZnO - x PDMS composites.

# 3.3 | Electrical characterization of (1 - x)ZnO – x PDMS composites

Figure 6A,B plots the complex plane of the room temperature impedance response (Z' vs Z'') for x = 0.00, 0.01, 0.03, and 0.05 in the (1 - x) ZnO - x PDMS composites. The magnitude of the bulk impedance response (given by the intercept of the semicircle with the Z' axis in the complex plane) is inversely proportional to the volume fraction of polymer which is both unintuitive and the reverse of the findings from a previous study of cold sintering applied to the ZnO-PTFE system. Secondly, the bulk imaginary impedance of the samples with nonzero amounts of PDMS are multiple orders

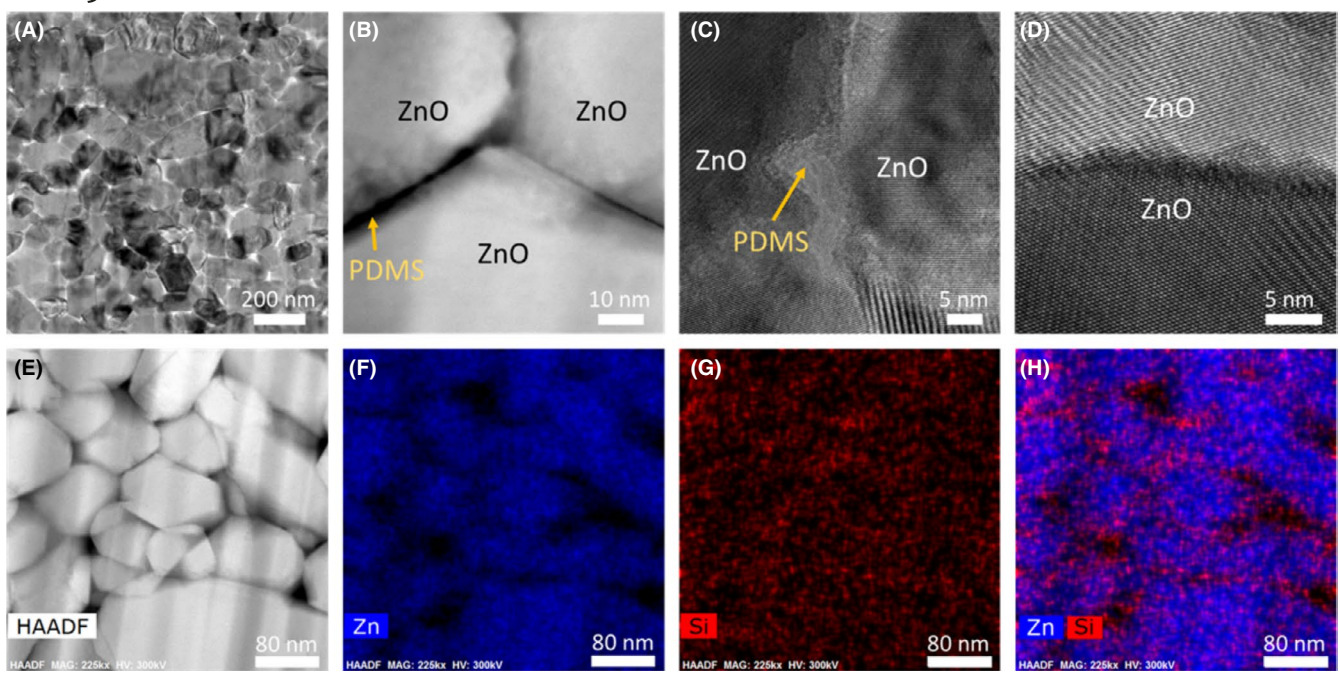


**FIGURE 5** (A-D) High-resolution TEM images of 0.97 ZnO – 0.03 PDMS composite at different magnifications (EDS mapping of (B) is available in Figure S3). EDS analysis of 0.97 ZnO – 0.03 PDMS composite with (E) A HAADF-STEM image, (F) EDS elemental mapping of zinc (Zn), (G) silicon (Si), and (H) both Zn and Si. EDS, energy dispersive spectroscopy; HAADF, high-angle annular dark-field; PDMS, polydimethylsiloxane; STEM, scanning transmission microscope; TEM, transmission electron microscopy

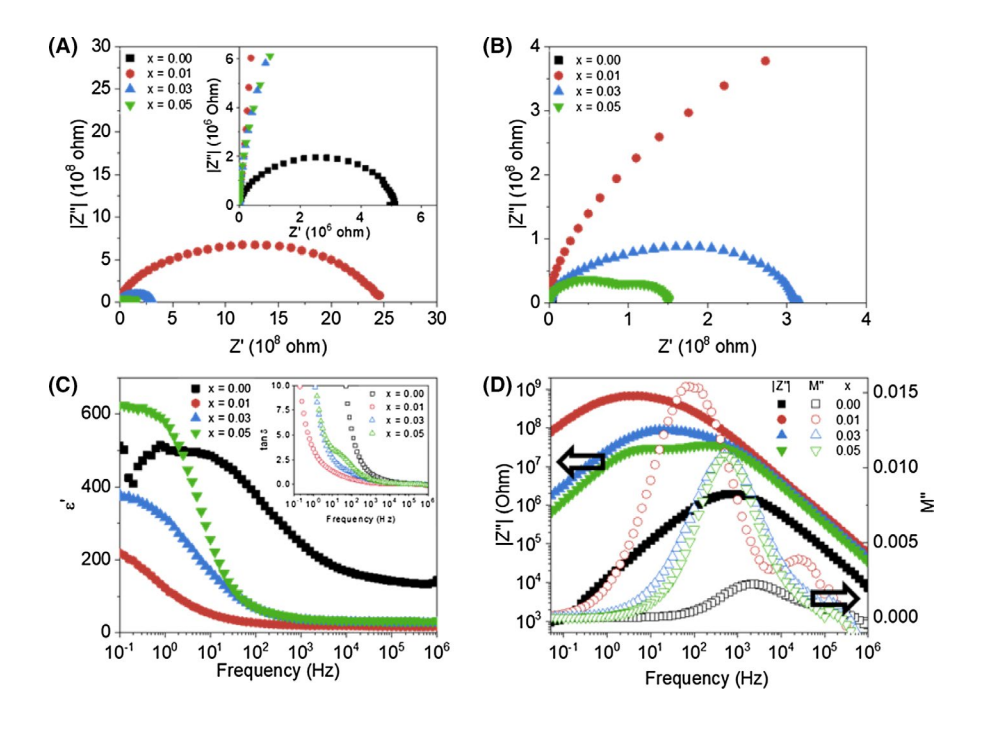


**FIGURE 6** (A and B) Impedance spectroscopy for (1-x) ZnO -x PDMS samples for x=0.00, 0.01, 0.03, and 0.05 presented as the Z-complex plane. The inset in (A) is magnification of the complex plane of x=0.00. (C) Real part of the permittivity ( $\varepsilon$ ') and dielectric loss tangent (tan  $\delta$ ) in inset as a function of frequency. (D) |Z''| (filled shapes) and M'' (open shapes) are plotted as a function of frequency. All measurements of polished samples with Pt electrodes and taken at 20°C with an amplitude of 0.5 V. PDMS, polydimethylsiloxane

of magnitude larger than that of pure ZnO; ZnO ( $10^6$  ohm), x = 0.01 ( $10^8$  ohm), x = 0.03 PDMS ( $10^7$  ohm), and x = 0.05 ( $10^7$  ohm). This indicates that the ZnO-PDMS composite is much less conductive than the pure cold sintered ZnO, as might be expected from the inclusion of a polymer lacking mobile charge carriers. <sup>56</sup> Thirdly, there appears to be a wide

dispersion in the time scales of the impedance responses measured as shown by the peaks in the modulus (M") and impedance (Z") plots vs frequency (Figure 6D). These modulus peaks occur at  $10^{3.3}$  Hz,  $10^{1.9}$  Hz,  $10^{2.7}$  Hz, and  $10^{2.7}$  Hz, for x = 0.00, x = 0.01, x = 0.03, and x = 0.05, respectively (note the identical peak frequency for x = 0.03 and x = 0.05).

Finally, in Figure 6C, we note that the relatively real part of the permittivity of the pure ZnO (x=0.00) in the high-frequency regime ( $\varepsilon'\approx 140$  at  $10^5$  Hz) is greater than the typically reported dielectric constant for a ZnO grain (~8.5).<sup>57</sup> This high "apparent" real permittivity can possibly be explained by charge accumulation at the ZnO grain boundaries after cold sintering. Similarly, recent studies of cold sintering mechanisms in ZnO report anomalously high concentrations of defects (eg, Zn<sup>o</sup><sub>i</sub> and  $V^o_O$ ) in proximity to the grain boundary.<sup>54</sup> Thus, the results of this study and those of the previously mentioned study suggest that a comprehensive study of CSP-ZnO impedance may serve to shed light on the relation between cold sintering mechanisms and their implications on grain boundary chemistry and properties.

The samples containing PDMS do not show a high permittivity in the high-frequency regime, with permittivity saturations much closer to the true dielectric constant of ZnO ( $\varepsilon' = 16.7, 27.6, \text{ and } 32.7 \text{ for } x = 0.01, 0.03, 0.05,$ respectively). If we assume that the previous attribution of the high-frequency  $\varepsilon'$  of cold sintered ZnO to a grain boundary charge accumulation is accurate, then the permittivity of the ZnO-PDMS samples implies a lack of space charge accumulation at the ZnO/ZnO interfaces in the composite compared to the pure polycrystalline sample fabricated via CSP. Previous reports of the permittivity of pure PDMS in the frequency range place the real part of the dielectric constant at about 3, meaning that the response measured here is likely not from any bulk PDMS response either.<sup>56</sup> We may also exclude the possibility of this effect arising from any space charge accumulation via electrode-composite interaction since the magnitude of the impedance larger than one would expect for a metal-electrode effect and the results were not changed when using a different metal electrode material (not presented here). Recalling the discussion of the effect of PDMS on the cold sintering of ZnO given in Sections 3.1 and 3.2, the permittivity measurements may be reconciled by considering the progressively smaller extent of ZnO-ZnO grain boundary interfaces as a consequence of PDMS decreasing the rate and extent of grain growth in the ZnO matrix. Thus, the ZnO grain boundaries no longer dominate the electrical response at high frequencies, rather, the response is driven more by the electrical response of the ZnO grains themselves. Furthermore, the permittivity of at low frequencies seems to be consistent with space charge accumulation at ZnO-PDMS interfaces, with increasing saturation  $\varepsilon'$  values with increasing volume fractions of PDMS. The dielectric loss tangent (tan  $\delta$ , Inset Figure 6C) offers further support for the above inferred effects of PDMS in ZnO. For pure ZnO (x = 0.00) the tan  $\delta$  rises rapidly at low frequency due to DC (direct current) conduction while the increase in tan δ is suppressed when PDMS is added as electrically insulating polymers reduce DC conduction.

The coating of the ZnO grains with electrically insulating PDMS is further supported by inspection of the relative peak locations of the modulus and impedance with respect to frequency. Gerhardt<sup>58</sup> demonstrated that simultaneous plotting of certain immittance formalisms helps to distinguish the difference in impedance responses due to long-range conduction compared to localized dielectric relaxations. Specifically, significant overlap or close proximity of M" and Z" peaks (plotted against frequency on a logarithmic scale) is indicative of long-range conduction in a material, which is observed here for pure cold sintered ZnO. In contrast, the large separation in immittance peaks indicates a localized dielectric relaxation, which is clearly observed for x = 0.01. The shift to a lower frequency response overall when PDMS is present suggests the same. For x = 0.03 and 0.05, a consistent Z" response between 1.5 and  $3 \times 10^8$  ohm with a peak at  $10^{2.7}$  Hz (~500 Hz) indicates that these volume fractions share similar electrical response mechanisms which differs from both the zero and one volume percent PDMS loading. The return to relatively close M" and Z" peaks implies that said response contains some extent of long-range conduction. Plotting the AC conductivity of these samples over the measured frequency range, and referencing the literature for data of neat PDMS (Figure S4), it becomes apparent that the conductivity of x = 0.03 and 0.05 (ca.  $3 \times 10^{-7} \text{ S} \cdot \text{m}^{-1}$ ) lie between that of pure ZnO  $(1.2 \times 10^{-5} \text{ S} \cdot \text{m}^{-1})$  and pure PDMS  $(2 \times 10^{-9} \text{ S} \cdot \text{m}^{-1})$ . Taken together, these observations suggest that the ZnO-PDMS composites regain some longrange conduction upon appreciable levels of PDMS (here x = 0.03 and 0.05) and that both ZnO and PDMS contribute to this response. The conduction pathway cannot be explicitly inferred from these measurements, but the impedance magnitudes and frequency range of the response suggest a ZnO/PDMS interfacial response. This also appears to be the origin to the initial observation that the real part of impedance, Z', is inversely proportional to the volume percentage of PDMS; the lowest fractions of PDMS lack the conduction mechanism present at the higher volume loadings. It is presently unclear specifically why this occurs at low volume fractions, but the densification kinetics presented above and observed microstructures show that the ZnO matrix is nearly completely sintered; likely hindering polymer dispersion and cross-linking in the composite.

Furthermore, one of the most salient features of the x = 0.05 complex impedance plot is the presence of two overlapping semicircles of similar impedance magnitudes (Figure 6B), indicating two distinct microstructural features with very similar resistivities. For x = 0.03, the presence of two semicircles is less obvious but the resulting asymmetric semicircular spectra still implies a mixed response. Inspection of Figure 6D, where Z'' is plotted as a function of log frequency, also shows that the peaks associated with

these two semicircles fall directly under the broad single peak observed in the x = 0.03 impedance spectra. As previously discussed, the magnitude and frequency of these aforementioned peaks make them likely due to ZnO/PDMS interfaces, so it follows that the two distinct peaks/semicircles in x = 0.05 may be attributed to two different types of ZnO/PDMS interfaces. Since the separation of the two responses is much clearer in the x = 0.05 samples than the x = 0.03 samples, the increased amount of PDMS seems to exacerbate the differences of these different interface types. Impedance spectroscopy was performed on these samples from room temperature (20°C) to -40°C with the heuristic assumptions that the x = 0.03 peak is a composite of the two x = 0.05 peaks and that these two responses can be accurately represented by an equivalent circuit of two constant phase elements, each parallel to a perfect resistor, such that the activation energy of each response could be extracted from the fitted data. A schematic of the equivalent circuit used to fit the data and the Arrheniuslike behavior is plotted in Figure S5 and extracted values presented in Table S2. The calculated activation energies of the two relaxations (semicircles) at low and high frequency are  $0.12 \pm 0.001$  eV and  $0.16 \pm 0.011$  eV, respectively. These are smaller values than the one observed for grain boundary in the conventionally sintered ZnO varistor,<sup>59</sup> but similar to those in cold sintered pure ZnO.<sup>2,54</sup> None of the other characterizations performed in this study could distinguish these distinct interfaces so future work will be needed in order to explore the types of interfaces that can arise in such sintered ceramic-dominated-thermoset polymer composites.

## 4 | CONCLUSION

In summary, we investigated the fabrication of the first ceramic-thermosetting polymer composites by the CSP, for high ceramic volume fractions (v/v >95%). All tested compositions of (1 - x) ZnO – x PDMS materials tested are densified as they have relative densities higher than 90% and surface areas smaller than 2 my<sup>2</sup>·g<sup>-1</sup>. Ceramics matrix was densified following a pressure solution creep mechanism. The presence of thermosetting polymers at the interface between two ZnO grains is limiting their grain growth and influencing grain anisotropy as ceramic-ceramic contacts are mainly favored in the direction of pressure. The addition of PDMS appears to replace ZnO-ZnO grain boundaries with ZnO/PDMS interfaces as evidenced by HR TEM and impedance spectroscopy. The bulk impedance response of the (1 - x) ZnO – x PDMS composites are up to three orders of magnitude larger than pure ZnO but are only one order of magnitude larger for x = 0.03 and x = 0.05. Two distinct interfacial relaxations can be identified but their physical

attributions remain tenuous. Changes in high-frequency permittivity for ZnO-PDMS composites compared to cold sintered ZnO can be attributed to physiochemical changes in the composite grain boundaries.

#### **ACKNOWLEDGMENT**

This work was supported by Murata Manufacturing Co., Ltd (AN), AFOSR grant no. FA9550-16-1-0429 (ZAG and CAR) and the National Science Foundation grant no DMR-1728634 (S-HB). We acknowledge Dr Tawanda J. Zimudzi for fruitful FTIR discussions. We acknowledge Prof. Zoubeida Ounaies and Dr Md Abdulla Al Masud for sharing their expertise on PDMS and for providing the Sylgard<sup>®</sup> cross-linking agent.

#### **ORCID**

Arnaud Ndayishimiye https://orcid. org/0000-0003-3853-8239 Clive A. Randall https://orcid.org/0000-0002-5478-2699

#### REFERENCES

- Guo J, Zhao X, Herisson de Beauvoir T, Seo JH, Berbano SS, Baker A, et al. Recent progress in applications of the cold sintering process for ceramic – polymer composites. Adv Funct Mater. 2018;28:1801724 (1–15).
- 2. Zhao X, Guo J, Wang K, Herisson De Beauvoir T, Li B, Randall CA. Introducing a ZnO–PTFE (polymer) nanocomposite varistor via the cold sintering process. Adv Eng Mater. 2018;20(7):1–8.
- Guo J, Berbano SS, Guo H, Baker AL, Lanagan MT, Randall CA. Cold sintering process of composites: bridging the processing temperature gap of ceramic and polymer materials. Adv Funct Mater. 2016;26(39):7115–21.
- Faouri SS, Mostaed A, Dean JS, Wang D, Sinclair DC, Zhang S, et al. High quality factor cold sintered Li<sub>2</sub>MoO<sub>4</sub>-BaFe<sub>12</sub>O<sub>19</sub> composites for microwave applications. Acta Mater. 2019;166:202–7.
- Induja IJ, Sebastian MT. Microwave dielectric properties of cold sintered Al<sub>2</sub>O<sub>3</sub>-NaCl composite. Mater Lett. 2018;211:55–7.
- Gyan DS, Dwivedi A. Structural and electrical characterization of NaNbO<sub>3</sub>-PVDF nanocomposites fabricated using cold sintering synthesis route. J Appl Phys. 2019;125:024103 (1–11).
- Ivakin YD, Smirnov AV, Tarasovskii VP, Rybal'chenko VV, Vasin AA, Kholodkova AA, et al. Cold sintering of ZnO ceramic in water medium: test demonstration. Glas Ceram. 2019;76(5–6):210–5.
- Guo J, Guo H, Baker AL, Lanagan MT, Kupp ER, Messing GL, et al. Cold sintering: a paradigm shift for processing and integration of ceramics. Angew Chem Int Ed. 2016;55(38):11457–61.
- 9. Guo H, Guo J, Baker A, Randall CA. Hydrothermal-assisted cold sintering process: a new guidance for low-temperature ceramic sintering. ACS Appl Mater Interfaces. 2016;8(32):20909–15.
- 10. Maria JP, Kang X, Floyd RD, Dickey EC, Guo H, Guo J, et al. Cold sintering: current status and prospects. J Mater Res. 2017;32(17):3205–18.
- Goglio G, Ndayishimiye A, Largeteau A, Elissalde C. View point on hydrothermal sintering: main features, today's recent advances and tomorrow's promises. Scr Mater. 2019;158:146–52.
- 12. Bouville F, Studart AR. Geologically-inspired strong bulk ceramics made with water at room temperature. Nat Commun. 2017;8:14655.

- Kähäri H, Teirikangas M, Juuti J, Jantunen H. Dielectric properties of lithium molybdate ceramic fabricated at room temperature. J Am Ceram Soc. 2014;97(11):3378–9.
- Kähäri H, Teirikangas M, Juuti J, Jantunen H. Improvements and modifications to room-temperature fabrication method for dielectric Li<sub>2</sub>MoO<sub>4</sub> ceramics. J Am Ceram Soc. 2015;98(3):687–9.
- Dargatz B, Gonzalez-Julian J, Guillon O. Improved compaction of ZnO nano-powder triggered by the presence of acetate and its effect on sintering. Sci Technol Adv Mater. 2015;16:025008.
- Berbano SS, Guo J, Guo H, Lanagan MT, Randall CA. Cold sintering process of Li<sub>1.5</sub>Al<sub>0.5</sub>Ge<sub>1.5</sub>(PO<sub>4</sub>)<sub>3</sub> solid electrolyte. J Am Ceram Soc. 2017:100:2123–35.
- Lee W, Lyon CK, Seo J, Lopez-Hallman R, Leng Y, Wang CY, et al. Ceramic – salt composite electrolytes from cold sintering. Adv Funct Mater. 2019;29:1807872:1–8.
- Seo J-H, Guo J, Guo H, Verlinde KS, Heidary DSB, Rajagopalan R, et al. Cold sintering of a Li-ion cathode: LiFePO<sub>4</sub>-composite with high volumetric capacity. Ceram Int. 2017;43(17):15370–4.
- Guo J, Guo H, Heidary DSB, Funahashi S, Randall CA. Semiconducting properties of cold sintered V<sub>2</sub>O<sub>5</sub> ceramics and Co-sintered V<sub>2</sub>O<sub>5</sub>-PEDOT:PSS composites. J Eur Ceram Soc. 2017;37(4):1529–34.
- Duffy DC, Mcdonald JC, Schueller OJA, Whitesides GM. Rapid Prototyping of microfluidic systems in poly (dimethylsiloxane). Anal Chem. 1998;70(23):4974

  –84.
- Eduok U, Faye O, Szpunar J. Recent developments and applications of protective silicone coatings: a review of PDMS functional materials. Prog Org Coatings. 2017;111:124–63.
- Chasse W, Lang M, Sommer J-U, Saalwächter K. Cross-link density estimation of PDMS networks with precise consideration of networks defects. Macromolecules. 2012;45:899–912.
- Mittal KL, Etzler FM. Adhesion in pharmaceutical, biomedical, and dental fields. Hoboken, NJ: Wiley; 2017.
- Jung S, Kim JH, Kim J, Choi S, Lee J, Park I, et al. Reverse-micelle-induced porous pressure-sensitive rubber for wearable human – machine interfaces. Adv Mater. 2014;26:4825–30.
- Mccall WR, Kim K, Heath C, La Pierre G, Sirbuly DJ. Piezoelectric nanoparticle – polymer composite foams. ACS Appl Mater Interfaces. 2014;6:19504–9.
- Pedraza E, Brady A-C, Fraker CA, Molano RD, Sukert S, Berman DM, et al. Macroporous three dimensional PDMS scaffolds for extrahepatic islet transplantation. Cell Transpl. 2013;22(7):1123–35.
- Li X, Li Y, Huang T, Zhang T, Liu Y, Yang B, et al. Organic sponge photocatalysis. Green Chem. 2017;19:2925–30.
- Al MA, Ounaies Z. Dielectric properties of dielectrophoretically aligned ZnO-PDMS Composites. *Proc. ASME 2016 Conf. Smart Mater. Adapt. Struct. Intell. Syst.* Stowe, VT, USA; 2016:SMASIS2016-9128.
- Meddeb AB, Tighe T, Ounaies Z, Lopez-pamies O. Extreme enhancement of the nonlinear elastic response of elastomer nanoparticulate composites via interphases. Compos Part B. 2019;156:166–73.
- 30. Guo J, Legum B, Anasori B, Wang K, Lelyukh P, Gogotsi Y, et al. Cold sintered ceramic nanocomposites of 2D MXene and zinc oxide. Adv Mater. 2018;30(32):1–6.
- Funahashi S, Guo J, Guo H, Wang K, Baker AL, Shiratsuyu K, et al. Demonstration of the cold sintering process study for the densification and grain growth of ZnO ceramics. J Am Ceram Soc. 2017;100:546–53.

- Belovickis J, Macutkevic J, Svirskas Š, Samulionis V, Banys J, Shenderova O, et al. Ultrasonic and dielectric relaxations in PDMS/ZnO nanocomposite. Phys Status Solidi Basic Res. 2015;252(12):2778–83.
- Belovickis J, Macutkevic J, Svirskas Š, Samulionis V, Banys J, Shenderova O, et al. Dielectric spectroscopy of polymer based PDMS nanocomposites with ZnO nanoparticles. Ferroelectrics. 2015;479(1):82–9.
- Barsoukov E, Macdonald JR. Impedance spectroscopy. Hoboken, NJ: John Wiley & Sons; 2005.
- Psarras GC. Conductivity and dielectric characterization of polymer nanocomposites. Phys Prop Appl Polym Nanocomposites. 2010:31–69.
- 36. Floyd R, Lowum S, Maria J-P. Instrumentation for automated and quantitative low temperature compaction and sintering. Rev Sci Instrum. 2019;90:055104 (1–8).
- 37. Ndayishimiye A, Tsuji K, Wang K, Bang SH, Randall CA. Sintering mechanisms and dielectric properties of cold sintered (1-x) SiO<sub>2</sub> x PTFE composites. J Eur Ceram Soc. 2019;39(15):4743–51.
- Pérez JMM, Pascau J. Image processing with ImageJ. Birmingham, UK: Packt Publishing; 2013.
- 39. Gratier J-P, Dysthe DK, Renard F. The role of pressure solution creep in the ductility of the Earth's upper crust. Adv Geophys. 2013;54:47–179.
- Urai JL, Spiers CJ, Zwart HJ, Lister GS. Weakening of rock salt. Nature. 1986;324:554

  –7.
- 41. Sengul MY, Randall CA, Van Duin ACT. ReaxFF molecular dynamics study on the influence of temperature on adsorption, desorption, and decomposition at the acetic acid/water/ZnO (1010) interface enabling cold sintering. ACS Appl Mater Interfaces. 2018;10:37717–24.
- Sengul MY, Randall CA, Van Duin ACT. ReaxFF molecular dynamics simulation of intermolecular structure formation in acetic acid-water mixtures at elevated temperatures and pressures. J Chem Phys. 2018;148:164506.
- 43. Sengul MY, Guo J, Randall CA, Van Duin ACT. Water-mediated surface diffusion mechanism enabling the Cold Sintering Process: a Combined Computational and Experimental Study. Angew Chem Int Ed. 2019;58(36):12420–4.
- Gorti S, Ware BR. Probe diffusion in an aqueous polyelectrolyte solution Probe diffusion in an aqueous polyelectrolyte solution. J Chem Phys. 1985;83:6449–56.
- 45. Renard F, Ortoleva P. Water films at grain-grain contacts: Debye-Huckel, osmotic model of stress, salinity, and mineralogy dependence. Geochim Cosmochim Acta. 1997;61(10):1963–70.
- 46. Socrates G. Infrared and Raman characteristic group frequencies. Chichester, West Sussex, England: John Wiley & Sons; 2001.
- 47. Bistricic L, Borjanovi V, Mikac L, Dananic V. Vibrational spectroscopy vibrational spectroscopic study of poly (dimethylsiloxane) ZnO nanocomposites. Vib Spectrosc. 2013;68:1–10.
- 48. Musat V, Tabacaru A, Stefan Vasile B, Surdu V-A. Size-dependent photoluminescence of zinc oxide quantum dots through organosilane functionalization. RSC Adv. 2014;4:63128–36.
- Rose S, Prevoteau A, Elziere P, Hourdet D, Marcellan A, Leibler L. Nanoparticle solutions as adhesives for gels and biological tissues. Nature. 2014;505:382–5.
- Liufu S, Xiao H, Li Y. Investigation of PEG adsorption on the surface of zinc oxide nanoparticles. Powder Technol. 2004;145:20–4.
- Ferreira OJB, Demétrio KB, dos Santos LAL. Nanostructured hydroxyapatite/polydimethylsiloxane composites obtained by reactive synthesis. Compos Part B Eng. 2017;121:152–61.



- 52. Srividhya M, Reddy BSR. Synthesis and characterization of polyimide containing PEG/PDMS amphiphilic conetworks by hydrosilylation: Correlation between structure and properties. J Polym Sci Part A Polym Chem. 2007;45(9):1707–26.
- 53. Santra RN, Mukunda PG, Nando GB, Chaki TK. Thermogravimetric studies on miscible blends of acrylate copolymer (EMA) and polydimethylsiloxane rubber (PDMS). Thermochim Acta. 1993;219:283–92.
- 54. Gonzalez-Julian J, Neuhaus K, Bernemann M, Pereira da Silva J, Laptev A, Bram M, et al. Unveiling the mechanisms of cold sintering of ZnO at 250°C by varying applied stress and characterizing grain boundaries by Kelvin Probe Force Microscopy. Acta Mater. 2018;144:116–28.
- German RM. Sintering theory and practice. New York, NY: Wiley; 1996.
- Ishaq S, Kanwal F, Atiq S, Moussa M, Losic D. Synthesis of three phase graphene/titania/polydimethylsiloxane nanocomposite films and revealing their dielectric and impedance properties. Ceram Int. 2019;45(7):8713–20.
- Levinson LM, Philipp HR. Oxide nonlinear conductors: a review. MRS Proc. 1990;195:639–57.

- 58. Gerhardt R. Impedance and dielectric spectroscopy revisited: Distinguishing localized relaxation from long-range conductivity. J Phys Chem Solids. 1994;55(12):1491–506.
- Lee J, Hwang JH, Mashek JJ, Mason TO, Miller AE, Siegel RW. Impedance spectroscopy of grain boundaries in nanophase ZnO. J Mater Res. 1995;10(9):2295–300.

#### SUPPORTING INFORMATION

Additional supporting information may be found online in the Supporting Information section.

**How to cite this article:** Ndayishimiye A, Grady ZA, Tsuji K, Wang K, Bang SH, Randall CA. Thermosetting polymers in cold sintering: The fabrication of ZnO-polydimethylsiloxane composites. *J Am Ceram Soc.* 2020;103:3039–3050. <a href="https://doi.org/10.1111/jace.17009">https://doi.org/10.1111/jace.17009</a>